Mantle rain towards the Earth's surface: a model for the internal cycle of water

Denis Andrault [1,*] and Nathalie Bolfan-Casanova [1]

[1] Laboratoire Magmas et Volcans, CNRS-OPGC-IRD, Université Clermont Auvergne, France

* Correspondence to denis.andrault@uca.fr

Abstract

The internal or deep water cycle controls the volume of the oceans at the surface of the Earth. The advent of subduction 2-3 billion years ago initiated the transport of water back to the Earth's interior. With one ocean mass injected into the deep mantle over the last 2-3 billion years, some mantle regions must have become saturated and thus turned into a deep source of water. The mantle transition zone (MTZ) between 410 and 660 km depths is unlikely to be a source of hydrous melt, because its minerals can integrate several thousand ppm of water. On the contrary, the low-velocity layer (LVL) lying above the 410 km-discontinuity is one such source. As proposed by the "Transition-Zone-Water-Filter Model", the LVL is ubiquitously formed by the global uplift of the hydrous MTZ as a counter flow of subduction of slabs into deeper regions. The seismic signature of the LVL is compatible with the presence of 0.5 to 1% melt. This melt is produced by dehydration melting during upwelling of the mantle transition zone (MTZ) containing 2200(300) ppm wt H_2O, which corresponds to 0.6 ocean mass stored today in the MTZ. Hydrous silicate melt can be gravitationally stable just above the 410 km discontinuity. We propose, here, that at the upper limit of the LVL it becomes buoyant, especially where the mantle is particularly hot and/or hydrous. Once it becomes buoyant, the melt can percolate rapidly upwards through the mantle. As a consequence, the olivine-bearing mantle (OBM) could be almost saturated in water, due to the presence of upwelling hydrous melt. On its path, the melt may be responsible for the seismic low-velocity zones at mantle depths of between 80 and 150 km. It could also be a source for refertilisation of the lithospheric mantle. Based on this model, there should be ~1.0 oceanic mass (OM) stored in the upper mantle today. Secular cooling of the mantle implies an increased capacity of the OBM minerals to store water. The related decrease of oceans' mass at the Earth's surface is estimated to ~20% per one billion years.

Introduction

Water is present at the surface of our planet, which made the development of life possible. Cosmochemical arguments indicate that the amount of initial water in the planet could have been equivalent to several oceanic masses (1 OM = $1.4.10^{21}$ kg H_2O) depending on the source (Marty, 2012; Piani et al., 2020). Regardless of the origin of water on Earth, the deep water cycle determines how much of the accreted water resides at the surface and how much is trapped in the planet's interior. In this article, we develop a model based on the water storage capacity of mantle minerals, which brings new constraints on the distribution of water in the Earth's mantle.

Modern plate tectonics has been operating for the last 2-3 billion years (Ga), during which water has been continuously introduced into the mantle at subduction zones. This regassing flux is particularly difficult to assess, since the different layers of a slab have heterogeneous water contents and the degree of serpentinization can vary as a function of the geological setting. Recent estimates converge to 1 to 2 10^{12} kg.yr^{-1} of water transported to the mantle at subduction zones, which equates to 0.7 to 1.4 times the OM every Ga. Still, most of the water is thought to escape from the slab, percolate into the mantle wedge and trigger arc volcanism. Only 30% to 40% of the initial slab water could be efficiently carried down to the deep mantle, resulting in a flux of 0.3 to 0.8 10^{12} kg.yr^{-1} H_2O or 0.2 to 0.5 OM/Ga (Rupke et al.,

2004; van Keken et al., 2011). With increasing depth, the hydrous minerals that are stable at the Earth's surface break down upon heating and their water content can eventually be incorporated as H point defects in nominally anhydrous minerals (NAMs) (Ohtani et al., 2018; Padrón-Navarta and Hermann, 2017). This evolution is facilitated by an increasing H-solubility in NAMs with increasing pressure. At depths greater than 410 km, the formation of wadsleyite and ringwoodite increases hydrogen solubility by about one order of magnitude (Bolfan-Casanova et al., 2000; Ferot and Bolfan-Casanova, 2012; Inoue, 1994; Ohtani et al., 2000). We note that a high water storage capacity does not necessarily imply a high water content. Still, the discovery of the first terrestrial ringwoodite, which contains 1.2 wt% H_2O, in a deep diamond, is a proof that water can reach the transition zone (Pearson et al., 2014).

Today, there is no consensus on the water content in the mantle transition zone (MTZ) with budgets varying from 0.3 to 3 OM (corresponding to ~1000 ppm to 1 wt% H_2O). A number of arguments have been proposed for or against high water contents based on different approaches: **(**i) elasticity measurements related to observed velocity jumps at 410 km depth invoke water contents that vary between 0.3 and 0.6 wt% H_2O (Buchen et al., 2018; Mao et al., 2008). (ii) Electrical conductivity yields controversial results from negligible water contents (Yoshino et al., 2008) to 0.1-0.2 wt% (Huang et al., 2005). (iii) It has also been proposed that 1-2 wt% H_2O are necessary to explain the viscosity contrast at 660 km depth, as inferred from the effect of water content on dislocation mobility in bridgmanite and ringwoodite (Fei et al., 2017). Of course, the water content of the MTZ does not have to be homogeneous. Hydrogen has a slow diffusion rate in the solid state (Demouchy, 2010; Hae et al., 2006), which can, however, be counterbalanced by a long residence time of a slab in the MTZ (Fukao and Obayashi, 2013).

A crucial geological setting for the internal cycle of water is the global low velocity layer (LVL) above the 410 km discontinuity (Revenaugh and Sipkin, 1994; Tauzin et al., 2010; Vinnik and Farra, 2007). It is unanimously interpreted as being due to dehydration melting (Revenaugh and Jordan, 1991; Song et al., 2004; Tauzin et al., 2010) and this is a strong indication that the transition zone is hydrous. Melting triggered by dehydration of the rising mantle occurs if the water content in the MTZ exceeds the water solubility of the olivine-bearing mantle (OBM). The LVL displays an average shear-wave velocity drop ($\delta Vs/Vs$) of about 4-5%, as reported in previous works, compared to the overlying OBM. Based on the experimental relationship between the Vs drop in hydrous peridotites and the amount of melt produced, the melt content in the LVL was constrained between 0.5 to 1.0 vol. % (Freitas et al., 2017; Xiao et al., 2020). The Transition Zone Water Filter model (Bercovici and Karato, 2003) is used as a mean of explaining the presence and fate of the melt in the LVL. It involves a continuous production of melt in the LVL associated with a water cycle around the transition zone, functioning in a closed system with only one input: water from the slab. The hypothesis is that, once formed atop the 410 km discontinuity, the dense melt travels laterally in the LVL until it freezes in contact with the cold slab and gets subducted (e.g. (Leahy and Bercovici, 2007)). The water would be released again after crossing the 660 km boundary and would diffuse up to the MTZ because water incorporation in bridgmanite is low (Bolfan-Casanova et al., 2003; Liu et al., 2021). Seismic low velocity zones below the 660-km discontinuity indicate inefficient penetration of water into the lower mantle (Durand et al., 2017; Liu et al., 2016; Schmandt et al., 2014). However, it should be relatively difficult to subduct the LVL melt because it is lighter than the MTZ (Matsukage et al., 2005; Sakamaki et al., 2006). In addition, the sustainability of a closed deep water cycle with water entering from the slab is questionable: if 0.2 to 0.5 OM were to be injected into the deep mantle every Ga (see above), the water content in the MTZ should have increased by 0.4-1.5 OM and hence the ocean level decreased of the same amount since the beginning of plate tectonics 2-3 Ga ago. This is obviously too extreme and incompatible with previous proposals of a 10-20% decrease in ocean mass since the Archean, based on hydrogen isotopes (Lecuyer et al., 1998; Pope et al., 2012) and geodynamic modeling (Flament et al., 2013).

At the other end of the deep water cycle, mid-ocean ridges are the main recognized geological setting where water is transferred from the mantle to the crust (in this study, water outgassing by arc

volcanism is not considered in the mantle budget because we only consider the flux entering the mantle beyond the formation of arcs, which is 0.3 to 0.8 10^{12} kg.yr^{-1} H_2O, as proposed by van Keken et al., 2011). The rate of basalt production is ~20 km^3.yr^{-1} (Cogne and Humler, 2006), corresponding to ~1.2 10^{11} kg.yr^{-1} of water assuming 2000 ppm water in basalts (Michael, 1988). This is at least twice less water than the lowest estimate of the water flux that is efficiently injected into the deep mantle by subduction. The difference of at least 0.2-0.7 10^{12} kg H_2O.yr^{-1} points out to the need of considering other possible sources of outgassing.

In this article, the strategy is to use quantitative constraints arising from mineral physics data, such as the water storage capacity of minerals, the effect of partial melting on seismic properties, the effect of composition (FeO and H_2O) on melt density, to develop a new model of the internal cycle of water. We explain how the LVL can play a major role in extracting water from the major reservoir constituted by the MTZ. The amount of water transported by the melt counterbalances the incoming water flow associated with the entry of slabs into the MTZ, resulting in a stable water balance for the MTZ. We investigate the conditions that can make buoyant a water-bearing melt formed in the LVL. Finally, we describe the possible implications of such "mantle rain" and compare them with various geological observations.

Maximum water solubility of the olivine-bearing mantle

The upper mantle is constituted of nominally anhydrous minerals (NAMs), which can accommodate water in their lattice in the form of OH defects. The major upper mantle phase, olivine, can incorporate more than 1000 ppm by weight of H_2O at high upper mantle pressures. The maximum water solubility in olivine is a function of pressure, temperature and oxygen fugacity. When the solubility limit is overpassed, an H_2O-rich phase appears, which can be a water-rich fluid at pressures lower than a couple of GPa or a water-bearing silicate melt at higher pressures (Kessel et al., 2015; Mibe et al., 2007). The phase equilibrium between the H_2O-bearing melt and the H-saturated olivine yields the following relations:

$$Mg_2SiO_4 + n\ H_2O <=> Mg_{1-n}H_{2n}SiO_4 + n\ MgO \quad (1)$$

$$[OH]^{olivine} = f_{H2O}{}^n \exp(\Delta G^{Ol}/RT) \quad (2)$$

f_{H2O} is the water fugacity (see details in Suppl. Material) and ΔG^{Ol} (ΔH^{Ol} - $T\Delta S^{Ol}$ - $P\Delta V^{Ol}$) the Gibbs free energy of the formation of H-defects in olivine, n is the exponent describing the incorporation mechanism. A best fit to the available experimental data (see (Ferot and Bolfan-Casanova, 2012) and references therein) yields the following values (assuming that H is substituting for Mg, hence n=1): (i) formation enthalpy ΔH^{Ol}= 47 kJ/mol, which compares well with previous reports of 37.1 kJ/mol (Bali et al., 2008) and 50 kJ/mol (Zhao et al., 2004), (ii) formation entropy ΔS^{Ol} increasing from 75 to 92 J/molK when pressure increases from 1 to 12 GPa, as described in (Bali et al., 2008; Smyth et al., 2006), and (iii) constant activation volume at ΔV^{Ol}=10.6 cm^3/mol (Kohlstedt et al., 1996; Mosenfelder et al., 2006). Note that the hypothesis of site substitution of H in Mg (n=1) or Si (n=2) site is necessary to extract the thermodynamic parameters from the solubility data, however, as demonstrated by (Yang, 2016) both sets of (n, ΔV) for n=1 or n=2 equally describe the data. Then, the maximum water-solubility limit in olivine can be calculated at all P-T conditions relevant to the upper mantle using Suppl-Eq. 1 (Suppl. Material) addressing the value of f_{H2O} in Eq. 2.

We can also calculate the H-content in the other mantle minerals coexisting with olivine under water-saturation conditions, using the published partitioning coefficients of H between olivine (Ol), enstatite (Opx), clinopyroxene (Cpx) and garnet (Gt). We adopt a H partition coefficients of 1 between olivine and garnet $D^{water}{}_{ol/gt}$ (Ardia et al., 2012; Novella et al., 2014), a $D^{water}{}_{opxx/ol}$ decreasing from 2 to 0.9 between Opx and olivine with increasing pressure from 2.5 to 9 GPa (Ferot and Bolfan-Casanova,

2012) and a $D^{water}_{cpx/opx}$ of 2 between Cpx and Opx (Demouchy et al., 2017). Finally, the well-known modal fractions of each of these phases in a peridotite-type upper mantle (Irifune and Isshiki, 1998) enables the calculation of the maximum water-solubility limit of the bulk olivine-bearing mantle (OBM) at any depth, following a given adiabatic temperature gradient (Fig. 1).

For a present-day mantle potential temperature (T_P) of ~1650 K (Katsura et al., 2010), the H_2O solubility limit of the OBM increases with depth from a few tens of ppm at the surface to ~1700 ppm wt at the 410 km seismic discontinuity. The effect of temperature is major, with a solubility limit decreasing by a factor of ~4 for T_P increasing from 1500 to 1950 K. It implies an increase of the water-storage capacity of the mantle with secular cooling that we will discuss later in more detail (see also (Dong et al., 2021)). We note that this calculation does not include possible effects associated with an increased water solubility limit in the first 100 km of the lithosphere (Green et al., 2014; Mierdel et al., 2007). In addition, the present model assumes conditions at which H_2O is the major hydrogen species in the melt (Druzhbin et al., 2021).

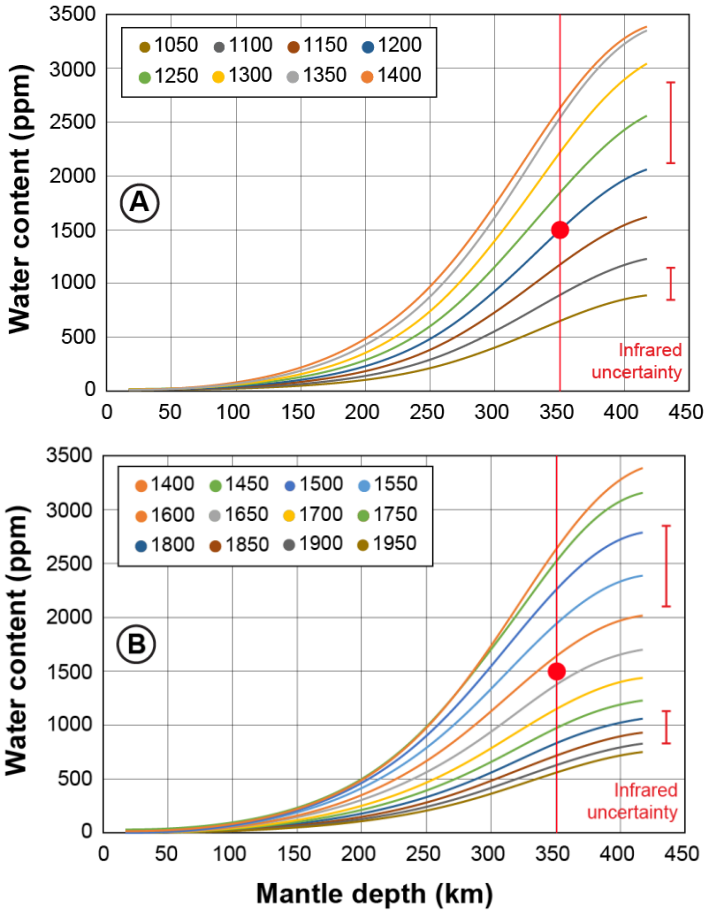

Fig. 1: Water-saturation limit of a peridotite-type mantle. Colored curves present the water saturation limits of the mantle as a function of depth along an adiabatic temperature gradient prevailing for mantle potential temperatures (T_P) from (**A**) 1050 to 1400 K and (**B**) 1400 to 1950 K (derived from (Ferot and Bolfan-Casanova, 2012)). A hydrous melt (or fluid) occurs at water contents above the saturation limit. At a given mantle depth, the saturation limit first increases with temperature up to T_P ~1400K and then decreases with further T increase. The latter effect is due to silicate dissolution in the melt and, therefore, a decrease in the activity of water in the hydrous silicate-melt at high temperature (see (Bali et al., 2008) and text). Uncertainty in the determination of the water content using infrared is +/- 15% (Ferot and Bolfan-Casanova, 2012). Red dot corresponds to 1500 ppm H_2O in the mantle at 350 km depth (see text).

H_2O-saturated solidus of upper mantle

The solubility curves of Fig. 1 can be inverted into H_2O-saturated solidii (Fig. 2), considering that a melt appears when, at any P-T condition above the second critical point of water, the water solubility limit of the OBM is overpassed. The "500 ppm H_2O-saturated solidus", for instance, is the P-T profile at which a water content above 500 ppm produces an incipient amount of melt saturated in H_2O. Due to the formalism of Eq. 2 (see Suppl. Material), the calculated H_2O-saturated solidii present a complex shape in the P-T diagram. In particular, they do not fall parallel to the dry-solidus (here we use that from

(Andrault et al., 2018), but the same observation would also stand for other works). Reasons for this are intrinsic to the thermodynamical properties of the minerals and hydrous melt. If we consider, for example, 1500 ppm of water in the mantle at 350 km depth (red dot in Fig. 1), such water content is higher than the water saturation limit, and would therefore yield the formation of a aqueous fluid, at temperatures below 1200 K (Fig. 1A) and hydrous melt above 1625 K (Fig. 1B). In contrast, the NAMs integrate 1500 ppm in the temperature range between 1200 and 1625 K. This yields a loop shape H_2O-saturated solidus in Fig. 2. We note that the effect of water on the thermodynamic parameters of the solid and melt may also induce mantle melting at temperatures just below the dry-solidus (Aubaud et al., 2004). In this case, however, neither the melt nor the solid residue would be saturated in H_2O. We do not report this effect in Fig. 2.

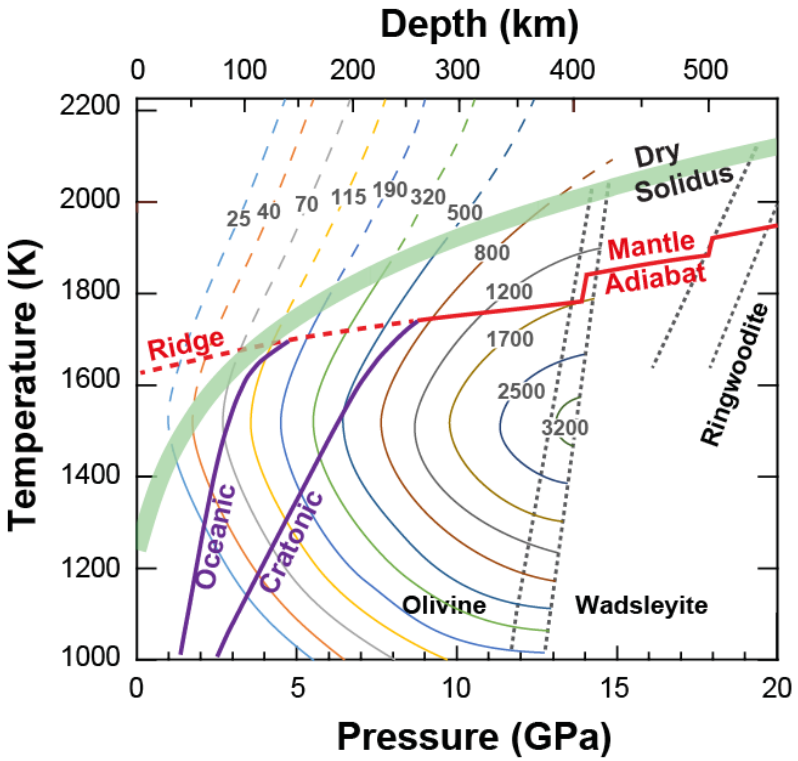

Fig. 2: The H_2O-saturated mantle solidii for water contents between 25 and 3200 ppm H_2O. The colored lines with associated water contents arise from the maximum water solubility displayed in Fig. 1. An H_2O-saturated melt appears on the left side of these curves (because water solubility decreases upon decompression) for H_2O-contents equal or superior to the reported number. We also report (i) the dry-solidus of chondritic-type mantle (green thick line (Andrault et al., 2018)) and (ii) the adiabatic temperature profile corresponding to T_P=1600-1650 K (Katsura et al., 2010). This figure does not consider the possible effect of a higher H_2O solubility limit in the lithosphere (Green et al., 2014; Mierdel et al., 2007; Sarafian et al., 2017). Uncertainty on water contents as in Fig. 1.

Continuous dehydration melting in the uprising mantle

A water content higher than the maximum water solubility induces the coexistence of water-saturated melt and solid residue. At a depth of 410 km, the OBM residue (produced by dehydration melting) should contain about 1700(200) ppm-wt H_2O (Fig. 2). This is much higher than the water content in the shallow source of mid ocean-ridge basalts (MORB), which contains between 50 and 250 ppm-wt H_2O at around 100 km depth (Michael, 1988). An appealing option to solve this discrepancy is that, during upwelling, the mantle H_2O-content decreases along with the water storage capacity limit (Ferot and Bolfan-Casanova, 2012) (Fig. 1). Hence, the mantle would remain partially molten at all depths (Hirschmann et al., 2005), until, at shallow depths, it finally reaches the value invoked for the MORB source. This seems incompatible with electrical conductivity measurements that do not favor a partially molten upper mantle between 180 and 350 km depth (Freitas et al., 2019; Toffelmier and Tyburczy, 2007). At least it implies that the fraction of melt should remain small. Based on the water-saturation profiles (Fig. 1), we calculate that the uprising by e.g. 10, 30 or 60 km from 410-km depth of the water-saturated mantle residue would produce ~0.07, ~0.25 or ~0.58 % of melt (colored dots in Fig. 3), respectively, assuming that the hydrous melt contains 6.5 wt% of water (see Table 1 and text below).

The same calculation can be performed for the uplift of the mantle residue from any mantle depth. The maximum amount of melt produced by an uplift of e.g. 30 km is ~0.37 wt%. This calculation shows that the amount of melt can be very small at any mantle depth if the melt that is regularly produced by dehydration melting is rapidly segregated from the uprising mantle. For a comparison, the seismic and electrical-conductivity anomalies observed between 80 and 150 km depth are compatible with more than 0.2% (Chantel et al., 2016) and between 0.3 to 2.0 wt% (Ni et al., 2011) of melt, respectively. At intermediate upper-mantle depths, the melt is buoyant and can travel upwards toward the Earth's surface. This could make its presence undetectable to geophysical measurements.

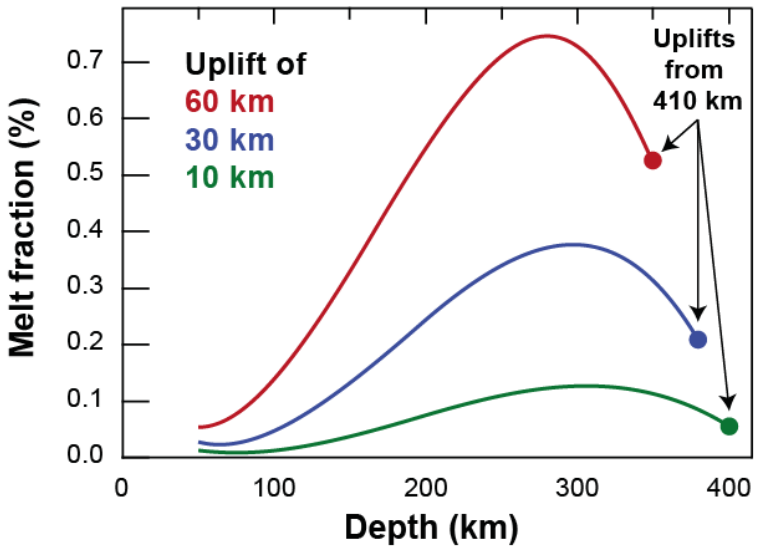

Fig. 3: **Dehydration melting in a rising upper mantle:** the uplift (i.e. adiabatic decompression) of a water-saturated residue induces continuous dehydration melting, due to a decrease of the water-saturation limit with decreasing mantle depth (Fig. 1). Here, we report the fraction of melt that can be expected at a given depth when a water-saturated mantle residue comes from 10, 30 or 60 km deeper, without loss of water during its ascent. Uplift from the 410 km seismic discontinuity are the colored dots. The curved shape with maxima around 275-300 km depth is due to the complex shape of the maximum water solubility limit in the mantle (Fig. 1). Uncertainties are +/- 15%, same as in Fig. 1.

Dehydration melting in the LVL: melt composition and phase diagram

The occurrence of a global low velocity layer (LVL) above the 410 km discontinuity (Revenaugh and Sipkin, 1994; Tauzin et al., 2010; Vinnik and Farra, 2007) is unanimously interpreted as being due to dehydration melting (Revenaugh and Jordan, 1991; Song et al., 2004; Tauzin et al., 2010). This is a strong indication that the transition zone is hydrous. Melting triggered by dehydration of the rising mantle occurs if the water content in the MTZ exceeds the water solubility of the olivine-bearing mantle (OBM). The LVL displays an average shear-wave velocity drop (δVs/Vs) between 4 and 5.6 %, as reported in previous works, compared to the overlying OBM. Based on the experimental relationship between the Vs drop in hydrous peridotite and the amount of melt produced, the melt content in the LVL was constrained between 0.5 to 1.0 vol. % (Freitas et al., 2017; Xiao et al., 2020). Dihedral angles are much lower (less than 10°) in the hydrous peridotite system at high-pressure (Freitas et al., 2017; Yoshino et al., 2007) and the amount of melt necessary to explain δVs/Vs is predicted to decrease at lower wetting angle (Hier-Majumder et al., 2014). Low wetting angles and low surface tension (Hier-Majumder et al., 2006; Yoshino et al., 2007) favor the fast mobility of the melt at grain boundaries. This is compatible with another major seismic observation in the LVL; no major melt ponds but instead a continuous global layer of partial melt that is not limited to regions associated with subduction or mantle plumes (Tauzin et al., 2010).

The composition of the water-bearing LVL-melt can be studied experimentally by reproducing an equilibrium texture between peridotite and 0.5 to 1 wt% melt. Analyses of thin veins of melt corresponding to ~2% partial melting indicate ~21.2 wt% FeO (recalculated after (Freitas et al., 2017)). However, the composition of liquids originating from low degrees of partial melting can be biased by

crystallization upon quenching, inducing an enrichment of incompatible elements in the residual melt. Alternative methods have been developed in order to determine the composition of incipient melts accurately, such as the iterative sandwich method (Dasgupta and Hirschmann, 2007), which yields a melt FeO-content of ~13.4 wt% for the LVL melt (Condamine and Frost, 2018). On the other hand, density measurements show variations of +21 and -16.5 kg/m^3 for every additional mol% FeO and wt% H_2O, respectively (Matsukage et al., 2005), in agreement with thermodynamical modeling (Freitas et al., 2017). As a result, a melt with an FeO-content of 11.6 wt% (used in (Matsukage et al., 2005)) or 13.4 wt% (ref. (Condamine and Frost, 2018), Table 1) would be neutrally buoyant at 350 km, at the top of the LVL, for H_2O contents of ~6 or ~7.1 wt% H_2O, respectively, in good agreement with previous work (Matsukage et al., 2005; Sakamaki et al., 2006). For modelling purposes, we use an average LVL-melt with reference FeO and H_2O contents of 12.5(1.0) and 6.5(1.0) wt %, respectively. We note that such FeO-content in the LVL of a peridotite-type mantle implies a solid-melt FeO partition coefficient D_{FeO}~0.65, which is compatible with D_{Fe}~0.56 proposed previously (Mibe et al., 2006).

Composition of LVL melts		SiO2	TiO2	Al2O3	FeO	MgO	CaO	Na2O	H2O	Total
Matsukage et al.	meas. (wt%	35.5		3.3	11.6	30.4	14.1		6.0	100.9
(2005)	norm. (wt%	35.2		3.3	11.5	30.1	14.0		5.9	100.0
	mol%	27.8		1.5	7.6	35.5	11.8		15.7	100.0
Condamine and	meas. (wt%	34.9	0.6	0.7	12.9	27.0	12.5	0.45	7.1	96.1
Frost (2018)	norm. (wt%	36.3	0.6	0.7	13.4	28.1	13.0	0.47	7.4	100.0
	mol%	28.1	0.4	0.3	8.7	32.4	10.8	0.35	19.0	100.0
Freitas et al. (2017)	meas. (wt%	29.7		2.6	21.2	2.6	9.0	0.07	13.6	78.8
F=2%	norm. (wt%	37.8		3.2	27.0	3.3	11.4	0.09	17.3	100.0
	mol%	27.6		1.4	16.4	3.6	8.9	0.06	42.0	100.0
Preferred values	wt%				12.5				6.5	

Table 1: **Composition of the LVL melt**: (Matsukage et al., 2005) reported the neutral buoyancy in the LVL of a melt containing 11.6 wt% FeO and 6.0 wt% H_2O. The concentration in major elements of the LVL-melt was further refined using the iterative sandwich method (Condamine and Frost, 2018). They refined a melt Fe-content of ~13.4 wt%, which should be neutrally buoyant in the LVL for an H_2O content of ~7.1 wt% (Freitas et al., 2017; Matsukage et al., 2005). In a later work, incipient melting was induced by dehydration melting while measuring the sound wave velocities under conditions relevant to the LVL (Freitas et al., 2017). In these experiments, however, crystallization of some olivine could have occurred upon quenching, making the primary melt composition difficult to retrieve. We calculate a solid-melt FeO partitioning coefficient D_{FeO}~0.65 between the LVL melt and the solid mantle residue.

We now draw the melting diagram of the hydrous mantle at 14 GPa (Fig. 4A). The solidus is the water storage capacity based on mineral properties (Fig. 1). At temperatures of 1500, 1650 and 1800 K, the maximum H_2O-content in the mantle is 2800(300), 1700(200) and 1060(100) K, respectively. For a mantle potential temperature (T_P) of 1650 K, the hydrous melt that is in equilibrium with the water-saturated mantle should contain ~6.5 wt% H_2O (Table 1). Using mass conservation we calculate the melt fraction in the LVL as a function of the bulk water content (Fig. 4B). A bulk-mantle water content of 2200 ppm (left vertical dashed line), 0.5 or 1 wt% (middle vertical dashed line) leads to the formation of 0.75, 5.2 or 13 wt% of melt in the LVL. The latter values are well above the 0.5-1% of melt required to account for low LVL velocities (Freitas et al., 2017), clearly indicating that the bulk water content of the LVL, and that of the MTZ as well, must be well below 1 wt%. One may argue that higher MTZ water-content could be possible, if the LVL-melt returns quickly to the MTZ (Leahy and Bercovici, 2007). However, (i) the LVL-melt is lighter than the MTZ (Fig. 5), with therefore no reason to sink through the 410-km discontinuity, and (ii) return of hydrous LVL-melt into the MTZ would indefinitely increase its water content, which does not seem sustainable. A higher water content in the MTZ is only

possible if the water-content in the LVL-melt has been underestimated in previous studies (Table 1). We will discuss the fate of the LVL-melt later in this article.

Finally, we draw the liquidus of this phase diagram passing through the melt composition at T_P=1650 K (~6.5 wt%) and assuming that it has the same, but inversed, curvature than that of the solidus (Fig. 5a). The resulting diagram suggests a slight decrease of the water content in the hydrous melt, from e.g. 7.4 to 5.1, when the potential temperature increases from 1500 to 1800 K, respectively. This indicates that for 2200 pm of water in the LVL, the melt fraction, Φ, increases from 0, ~0.75 and ~2.3 %, when temperature is 1500, 1650 and 1800 K, respectively.

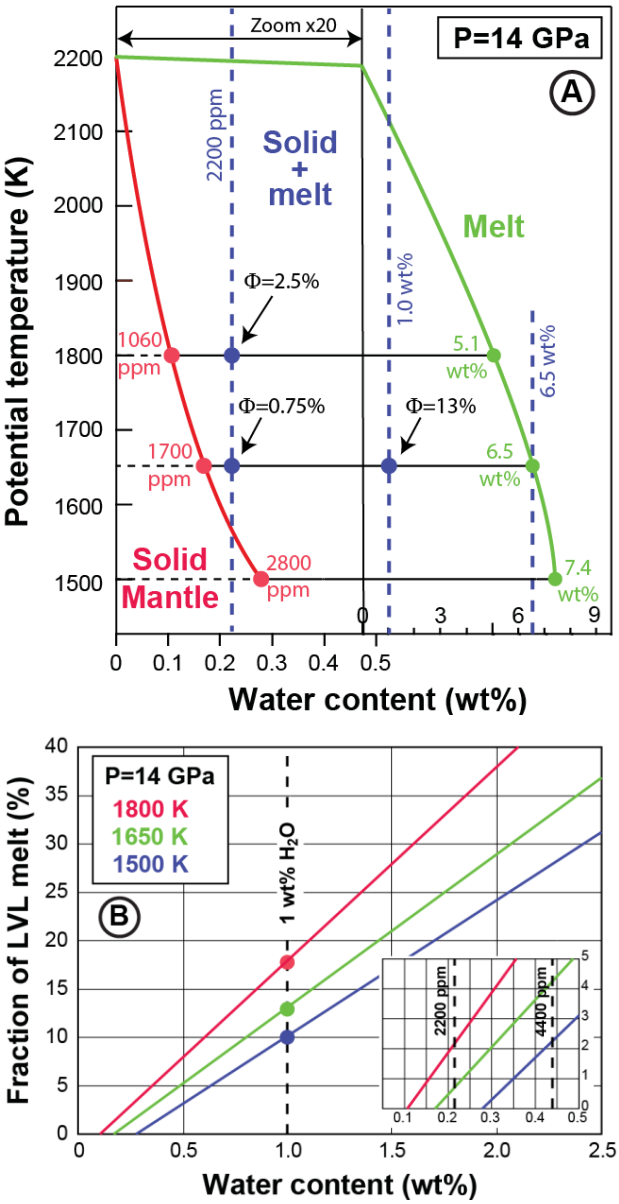

Fig. 4: (A) Phase diagram relevant to dehydration melting of the mantle: above the 410 km depth discontinuity (~14 GPa), exceeding the maximum water storage capacity of peridotite induces dehydration melting. At a mantle potential temperature (T_P) of 1650 K, the solid mantle can store a maximum of ~1700 ppm H_2O (Fig. 1) and the melt contains ~6.5 wt% H_2O (Table 1). It results that a bulk water content of 2200 ppm (left vertical dashed line) leads to the formation of 0.75% of melt, in agreement with seismic observations of the low-velocity layer (Freitas et al., 2017). Thus, the melting diagram is mainly built using constraints from previous reports. Alternatively, a bulk water content of 1 wt% (middle vertical dashed line) would yield 13% melt. At T_P=1800 K, a bulk water content of 2200 ppm would produce 2.5% of melt containing 5.1 wt% H_2O. This diagram shows that mantle heterogeneities of temperature and water-content affect significantly the degree of partial melting and the melt composition. Uncertainty on water contents is same as in Fig. 1. **(B) Fraction of LVL-melt**: based on the solidus and liquidus profiles, we calculate, from Fig. 4A, the fraction of melt that must be present in the LVL based on bulk mantle water content and for T_P of 1500, 1650 and 1800 K. Inset is a zoom of the melt fraction at low water contents. Uncertainty on the melt fraction is estimated to ~25%.

Melt-Mantle density contrast

The fate of the LVL-melt is primarily controlled by the melt-mantle density contrast ($\Delta\rho = \rho_{melt}$-ρ_{mantle}). A melt-mantle density crossover (that is where both densities of solid and melt become equal), occurs around the 410 km depth corresponding to ~14 GPa (Matsukage et al., 2005; Sakamaki et al., 2006) (Fig. 5a), due to (i) the higher compressibility of the melt, compared to the solid mantle, (ii) the absence of a major phase transition in mantle minerals above the 410 km discontinuity, and (iii) the

preference of FeO for the melt. Based on the equations of state and the dependence of the melt density on its FeO and H_2O contents (Jing and Karato, 2012; Matsukage et al., 2005), we recalculate the density contrast as a function of depth for various possible melt compositions (Fig. 5a). As expected, there is a maximum in the density contrast just above the 410 km discontinuity that then decreases with decreasing depth. In addition, we calculate that small variations in the FeO (+/- 3 wt%) and H_2O (+/- 2 wt%) contents can significantly affect the mantle depth at which neutral melt-mantle buoyancy is achieved.

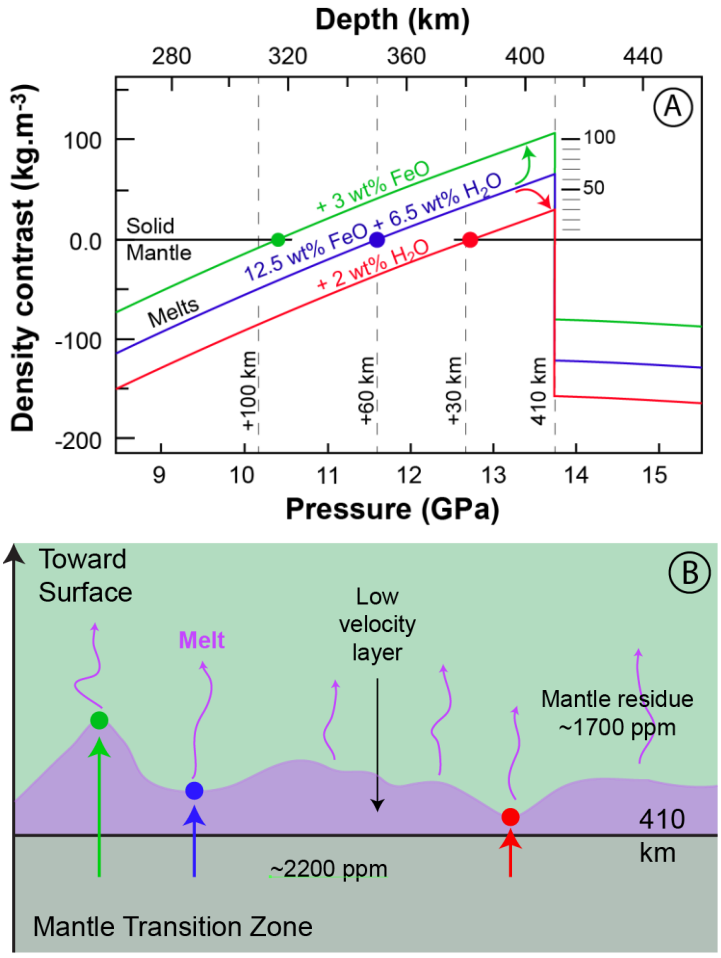

Thus, variations in melt composition can create variations of the thickness of the LVL (ΔZ_{LVL}). Indeed, the top of the LVL is the point of neutral melt-mantle density (red, blue and green dots in Fig. 5a) and further uprising of the mantle beyond this limit yields a buoyant melt, which upward migration is forced by gravity. A melt composition enriched in iron, by e.g. 3 wt%, yields a denser melt that is gravitationally stable across a broader region (from 410 to ~320 km depth, up to the green dot in Fig. 5a), thus implying an LVL which is thicker, by e.g. +40 km, compared to the mean mantle, which melt is gravitationally stable up to ~60 km above the 410 discontinuity (blue dot in Fig. 5a). In

Fig. 5: (A) Melt-Mantle density cross-over. Because melts have a higher compressibility compared to the solid mantle, the density difference between melt and solid increases with increasing depth, and the melt eventually becomes denser than the solid between the neutral buoyancy depth and the 410 km depth, at the olivine-wadsleyite phase transition. This depth interval (ΔZ_{LVL}) defines the thickness of the LVL. Neutral melt-mantle buoyancy is expected at the upper limit of the LVL, which is seismically observed 60 km in average above the 410 km discontinuity (blue dot). For a mantle of peridotite composition, the LVL-melt should contain 12.5 wt% FeO and 6.5 wt% H_2O (blue line, Table 1). The melt density changes significantly as a function of its FeO (green line) and H_2O (red line) contents (Matsukage et al., 2005; Sakamaki et al., 2006). Thus, the thickness of the region where the melt is denser (within ΔZ_{LVL}), can vary laterally inside the mantle due to heterogeneities in temperature and composition (see text). Depending on their composition, melts can be buoyant (less dense) at depths shallower than the green, blue or red dot. For comparison, density of the OBM at 410 km depth is ~3500 $kg.m^{-3}$. Uncertainties are detailed in previous works (Matsukage et al., 2005; Sakamaki et al., 2006) **(B) The "mantle-rain" model** proposes that the LVL-melts rise upward through the mantle once they reach the upper limit of the LVL. Melts migration occurs vertically and laterally along grain boundaries. The observed regional variations of the LVL-thickness can be explained by mantle heterogeneities in FeO, H_2O contents and temperature, which induce LVL-melts that are relatively denser (green dot) or lighter (red dot), compared to the typical LVL-melt (blue dot, Table 1). Still, any melt composition becomes buoyant above a given mantle depths (Fig. 5a).

contrast, a melt enriched in H_2O, by e.g. 2 wt%, yields a lighter melt that is gravitationally stable up to 30 km only above the 410 km discontinuity (red dot in Fig. 5a). Chemical variations of the melt can be induced by mantle heterogeneities in temperature, water content or even fertility. They can induce variations of the LVL thickness from ~30 to ~100 km that are compatible with seismological observations (Revenaugh and Sipkin, 1994; Tauzin et al., 2010; Vinnik and Farra, 2007).

Knowing the melting diagram of hydrous peridotite (Fig.4a), the manner in which the variation in mantle composition and temperature affect the density of the LVL melt can be assessed by constraining the melt fraction (Fig.4b). Indeed, given that the 410 km discontinuity is well explained globally by a peridotite (or pyrolite) mantle, there is no reason at this stage to invoke other components such as eclogite or sediments.

(i) Since water is an incompatible compound, a local increase of the water content in the MTZ would induce a higher degree of partial melting in the LVL (Fig. 4b). We determine that twice more water in the MTZ than the value of 2200 ppm would produce ~6 times more LVL-melt (~4.4 wt%, see inset of Fig. 4b). Such melt would contain the same amount of H_2O (fixed at the liquidus, Fig. 4a), but a lower FeO-content (reduced by ~1% compared to 6.5 wt%; Table 1), according to mass conservation $[FeO]_{Melt}=[FeO]_{Mantle}/(\Phi+(1-\Phi)D_{FeO})$, where Φ is the melt fraction and using D_{FeO}~0.65, the solid-melt FeO partition coefficient. As a result, such melt would be ~0.2% lighter (+21 kg/m^3 for every additional mol% FeO (Matsukage et al., 2005)), compared to the melt formed from a mantle containing 2200 ppm H_2O. Similarly, a bulk 1 wt% H_2O would produce 13 wt% of LVL-melt (see Fig. 4b) with ~5% less FeO and a density lowered by ~1%. The mantle residue also loses some Fe with increasing Φ, however, to a much lesser extent. Altogether, bulk water contents of 4400 ppm or 1 wt% imply a decrease of ~6.3 and ~36 kg.m^{-3}, respectively, from a melt-mantle density contrast of ~65 kg.m^{-3} at the base of the LVL for a water content of 2200 ppm H_2O (Fig 5a). This would yield a LVL up to ~30 km thinner, compared to the average mantle.

(ii) The mantle could also present variations in its fertility, implying significant heterogeneities in FeO-content, which incompatibility and molecular weight have important consequences on melt density, as we have seen. A reduction by 10% (from e.g. 8.0 to 7.2 wt% FeO) in the FeO content of the mantle would result in a stronger decrease of the melt FeO content, compared to that of the residue (due to $D_{Fe}^{Solid/Melt}=0.65$), and a decrease of the melt-mantle density contrast by 0.8% or ~28 kg.m^{-3} (Matsukage et al., 2005). This would yield a LVL ~30 km thicker, compared to the average mantle.

(iii) A locally higher mantle temperature would increase Φ (Fig. 4b). Such LVL-melt would be depleted in both H_2O and FeO, compared to mean mantle conditions as incompatible elements get diluted with increasing melt fraction. It is difficult to tell which of the two opposite effects (increasing FeO content or increasing H_2O content) dominates the melt-mantle density contrast. The imprecise shape of the liquidus in Fig. 4a yields a large uncertainty on Φ as a function of temperature. However, the effect of bulk water content could be significant, as illustrated by the change from 0.75 to 2.5 wt% of melt when T_P increases from 1650 to 1800 K, for a bulk H_2O-content of 2200 ppm (Fig. 4b).

(iv) Finally, the presence of carbonate in the LVL melt cannot be discarded. Carbonates are subducted to great depths and are known to react to form diamond in the transition zone (Pearson et al., 2014; Shirey et al., 2021). If present in the melt, C in the form of CO_3^{2-} is expected to increase the melt buoyancy relative to the surrounding mantle. Still, carbonates may more likely be present at depths shallower than ~150 km where the oxygen fugacity is higher (Stagno et al., 2013).

Overall, mantle heterogeneities in FeO and H_2O contents and possibly also temperature and CO_2-content appear to have a significant effect on the melt buoyancy, especially in the shallow part of the LVL where the melt-mantle density contrast is small (Fig. 5a). We acknowledge important uncertainties in the amplitude of the melt-density dependence on FeO, H_2O, CO_2 contents and temperature. However,

the trends described above are qualitatively correct and, therefore, mantle heterogeneities could be a major controlling parameter of the LVL-thickness.

Fate of hydrous-melt in the upper mantle

Overall, we expect the production of water-rich melts to be widespread in the OBM: not only the LVL could be a continuous source of buoyant melts, but the uprising residual mantle is expected to dehydrate progressively on its way toward the surface (Fig. 3). While the vertical mobility of the melt is certainly triggered by a melt being more buoyant with increasing elevation from the 410 km discontinuity (Fig. 5a), lateral migration is also facilitated by several parameters: (i) a low dihedral angle in the hydrous peridotite system at high pressure (Yoshino et al., 2007) (ii) significant grain to grain surface energy between silicate minerals, ~4 J/m^2 for olivine (Swain and Atkinson, 1978), though unfortunately poorly constrained in the presence of majoritic garnet, the second major phase at high upper-mantle depths and (iii) a major relaxation of the surface energy under hydrous conditions (de Leeuw et al., 2000). Large-distance melt propagation has already been proposed for the LVL-melt above the 410 km discontinuity (Leahy and Bercovici, 2007). Widespread circulation of metasomatic agents is also recognized in the cratonic lithosphere (O'Reilly and Griffin, 2013). We argue that a similar process also occurs within the convecting mantle and it is possible that chemical reactions favor mantle refertilization. As observed in nature, the percolation of hydrous melt into a mantle region that is not saturated in water would induce hydration of NAMs, drying out the melt and inducting its solidification (Denis et al., 2015; Doucet et al., 2014; Le Roux et al., 2007). Over geological time, the travelling melts can resolve at least partially the heterogeneity in water content between the different mantle regions. In this way, all mantle regions (even those that do not undergo dehydration melting upon uprising) could achieve a water content close to the saturation limit. For further modeling of the total water content in the upper mantle, we consider that the minerals of the OBM carry an amount of water that is close to the water saturation limit (Fig. 1).

On its way through the OBM, the buoyant hydrous melt eventually meets a critical depth where it decomposes into a mixture of volatile-bearing fluid and silicate-melt (Kessel et al., 2015; Mibe et al., 2007). The appearance of a fluid (Gaillard et al., 2008; Hirschmann, 2010) as well as the local accumulation of a viscous silicate-melt (Chantel et al., 2016; Priestley and McKenzie, 2013) could produce the low velocity zones (LVZ) detected by seismic and electrical conductivity measurements. The range of depths between 80 and 150 km where LVZs are detected (e.g. (Debayle and Ricard, 2012; Kawakatsu et al., 2009)) is compatible with the P-T conditions, around 3.8 GPa and 1273 K, at which the second critical end point was reported in the peridotite-H_2O system (Mibe et al., 2007). It is therefore appealing to make a causal link between the “mantle rain” and the LVZs. A major observation that needs to be taken into account is that the LVZ seismic and electrical-conductivity anomalies become weaker and deeper with increasing plate age (e.g. (Debayle et al., 2020)), while we expect ubiquitous upwelling of the melt from the LVL. A greater impact of the melt in young geological settings could arise from two major factors: (i) less hydrous melt reaches old compared to young lithospheres. The mantle underneath mid-ocean ridges is uprising and, therefore, the mantle residue is expected to undergo continuous dehydration melting on its path (Fig. 3). The hydrous-melt produced this way is added to the melt coming from the LVL (left side of Fig. 6). Alternatively, the mantle underneath an old lithosphere should be either stagnant (in depth) or sinking. Thus, no melt is produced by dehydration-melting upon decompression. Now if we consider that the regions where the mantle is sinking, one can expect that it would react and stop the LVL-melt at mid upper-mantle depth due to mantle rehydration (right side of Fig. 6). (ii) Young oceanic crust presents a much steeper temperature gradient in the first 100-150 km depth, compared to the continental crust. By comparing these temperature profiles and the mantle solidus, it appears that the formation of a water-saturated melt evolves progressively from ~150 ppm at

100-150 km depth, to ~700 ppm H_2O at 250-300 km depth, for young oceanic to old continental settings, respectively (Fig. 2). This denotes a larger impact of water in the young lithosphere.

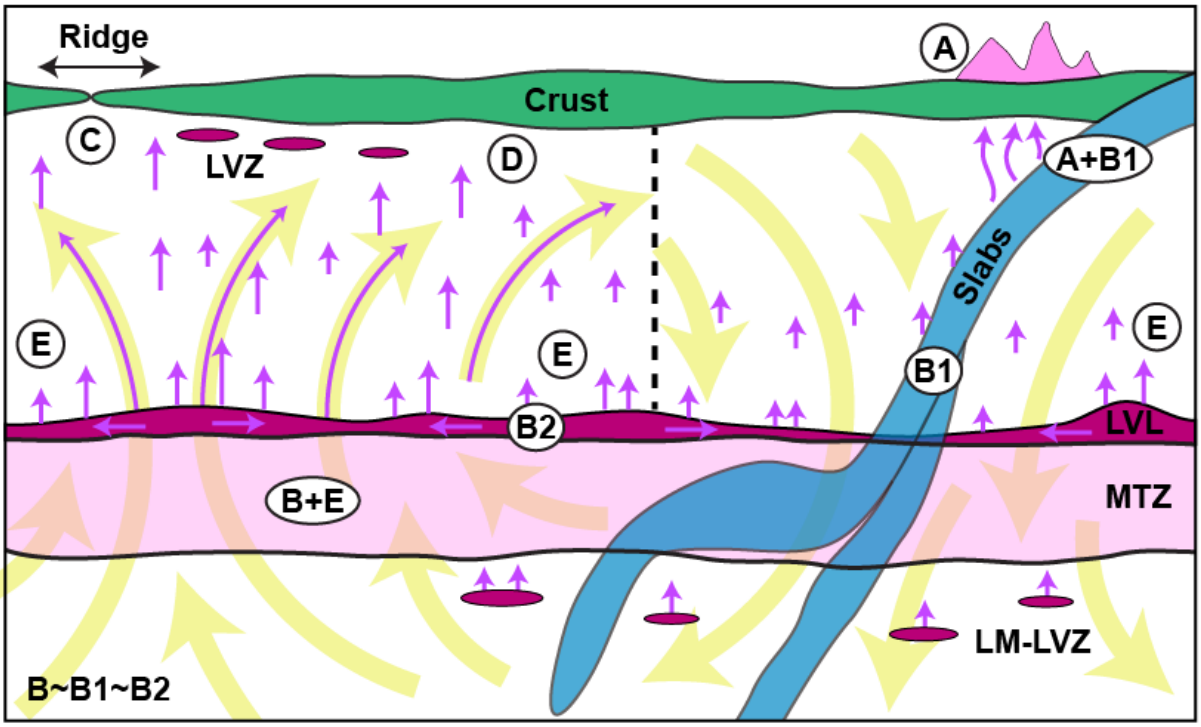

Fig. 6: Internal cycle of water and the mantle rain model. The mantle convects upward or downward in left and right parts of the diagram, respectively. Upward movement should dominate, though, in order to balance the inflow of slab (blue) into the deep mantle. Upon uprising of the water-rich MTZ material (light pink) and crossing of the 410 km mineralogical discontinuity, the mantle becomes water-saturated and dehydration melting produces the LVL-melt (dark pink layer). In addition, the uprising of the mantle residue continuously produces a water-bearing melt (curved pink arrows, Fig. 3). Above the upper limit of the LVL, the melt is buoyant and rises toward the surface (linear pink arrows, Fig. 5). Migration of the hydrous melt should take place in all directions, due to low surface tension; for clarity, lateral melt movements are not represented in this figure, except in the LVL. In mantle regions that are sinking, chemical reactions with the travelling hydrous melt is expected to hydrate mantle NAMs. Similar reactions occurring in the lithospheric mantle (point D) can produce mantle refertilisation and eventually intraplate volcanism. (A+B1) is the inflow of water at subduction zones; ~1-2 10^{12} kg.yr^{-1} but only (B1) penetrates the deep mantle; 0.3-0.8 10^{12} kg.yr^{-1}. (B2) is the water contribution to produce the LVL-melt: 0.5(0.2) 10^{12} kg.yr^{-1}. (C) is the outflow of water at the ocean ridges; ~0.1 10^{12} kg.yr^{-1}. (B2) should roughly equal (C+D), with (D) the water flux into the lithosphere: 0.2-0.7 10^{12} kg.yr^{-1}. While (A) to (D) are water fluxes, (E) is the steady water content in the solid upper mantle. Considering that the upper mantle is almost saturated in water yields a total water content of 8.5(0.8) 10^{20} kg H_2O or 0.6(0.1) mass of the oceans. Calculations are detailed in the main text and captions of other figures. This cycle assumes a constant amount of water in the lower mantle and in the core. We note that some dehydration melting may occur below the 660 km and induce low seismic-velocity zones (LM-LVZ).

The transfer of melts and fluids enriched in incompatible and volatile elements to the lithospheric mantle may contribute to its refertilisation. In addition to well identified, hydrous metasomatism in mantle xenoliths from the cratonic mantle (Doucet et al., 2014; Le Roux et al., 2007), the presence of a few percent of pyroxenite is often invoked to explain the trace element and isotopic composition of mid-ocean ridge basalts (MORBs) originating from the oceanic mantle (Lambart et al., 2009). The hydrous melts originating from the transition zone could also help explaining the occurrence of less well-known magmatism. For example, the presence of residual fluids under-plating the crust could trigger the

formation of petit-spot volcanoes (Machida et al., 2017). Hydrous plumes coming from the MTZ have also recently been invoked to explain continental magmatism such as continental flood basalts beneath China (Kuritani et al., 2019; Wang et al., 2015), and beneath the Turkish-Iranian plateau (Soltanmohammadi et al., 2018). It is also notable that only a few identified mantle plumes (Liu et al., 2018; Vinnik and Farra, 2007; Zhang et al., 2018) come from great depth (Courtillot et al., 2003).

Water budget in the present-day deep mantle

In mantle regions subjected to continuous upwelling, melt is continuously formed in the LVL, while a partially depleted, but still water saturated, residue proceeds upwards (Bercovici and Karato, 2003). On a global scale, an incoming flow of ~2.5 10^{11} $m^3.yr^{-1}$ of subducted slab material (Wen and Anderson, 1995) through the MTZ implies an average uplift of ~0.6 $mm.yr^{-1}$ across the whole 410 km discontinuity. In order to induce dehydration melting, the water content in the transition zone needs to be higher than the maximum storage capacity of the OBM, which is 1700(200) ppm H_2O at 410 km for a mantle potential temperature of 1650 K (Fig. 1, see details in Suppl. Material). In addition, some water is carried by 0.5 to 1% of LVL melt containing 6.5(1) wt% H_2O. This represents an additional 300 to 700 ppm (thus, 500(200) ppm) H_2O, yielding a total mantle content of 2200(300) ppm H_2O (Fig. 4) to explain the seismic velocity drop in the LVL. We now consider that the average water content in the MTZ is comparable to that in the LVL (2200(300) ppm), which is only ~30% higher than the maximum solubility limit of the mantle (1700(200) ppm) in the LVL. This assumption implies that there is no accumulation of melt in the LVL, but instead continuous melt formation by dehydration melting and escape by *Mantle Rain* of a same amount of LVL-melt. Here, we evaluate what are the consequences of this assumption: (i) if the water content of the mantle uprising from the MTZ would be lower, between 1700(200) and 2200(300) ppm water, then there would still be dehydration melting. There would be less LVL-melt produced for a same amount of uprising MTZ material. This would lower the fluxes of LVL-melt out of the LVL and loss by uprising. (ii) Alternatively, more than 2200(300) ppm water in the MTZ would produce a fraction of LVL-melt higher than expected from the comparison between experiments and seismic data. This could be accommodated by the *Mantle Rain* model with a greater flux of uprising LVL-melt. Still, it should be compensated by a higher influx of water in the MTZ, which does not seem to be available (see text above and Fig. 6). It makes it unreasonable a MTZ water content significantly higher than 2200(300) ppm. In summary, slight variations of the MTZ water content away from the average value of 2200(300) ppm does not significantly change either the *Mantle Rain* model or the upper mantle water balance estimate that we develop below. We note that this value is far below the level of water saturation in MTZ, because wadsleyite can include up to 5 times more hydrogen than olivine at these P-T conditions (Ferot and Bolfan-Casanova, 2012). Based on the average value of 2200(300) ppm, the MTZ should contain 8.5(0.8) 10^{20} kg of water, corresponding to 0.6(0.1) OM.

The continuous rise of the water-bearing MTZ material by ~0.6 $mm.yr^{-1}$ corresponds to a total of ~2.0(0.3) 10^{12} $kg.yr^{-1}$ H_2O crossing upwards the 410 km discontinuity. This value is significantly larger than the 0.3 to 0.8 10^{12} $kg.yr^{-1}$ H_2O injected in the deep mantle by subduction ((van Keken et al., 2011); B1 in Fig. 6). Instead, it is the flux of water producing the LVL-melt, about 0.5(0.2) 10^{12} $kg.yr^{-1}$ (B2 in Fig. 6), that is well compatible with the flux of water entering the MTZ by subduction. This indicates that the production of LVL-melt is primarily triggered by the amount of deeply subducted water. On the other hand, the origin of the water present in NAMs uprising to the LVL cannot come from the subducted water. In the framework of global convection, NAMs are expected to cross the 410 km boundary in both directions and, for this reason, their contribution to the water transfer through the 410 km boundary is balanced. By analogy, the situation is comparable to the presence of incompatible elements in peridotite; they do not come from the subduction of MORBs. The water content of NAMs sinking through the 410 km discontinuity is unknown. However, it could be close to the NAMs saturation limit due to reaction with hydrous-melt present in the upper mantle (see above). In addition, they cross the water-saturated

LVL and could react there with the water-bearing melt. For this reason, we consider that the water content of NAMs in the upper mantle as a constant (contribution E in Fig. 6).

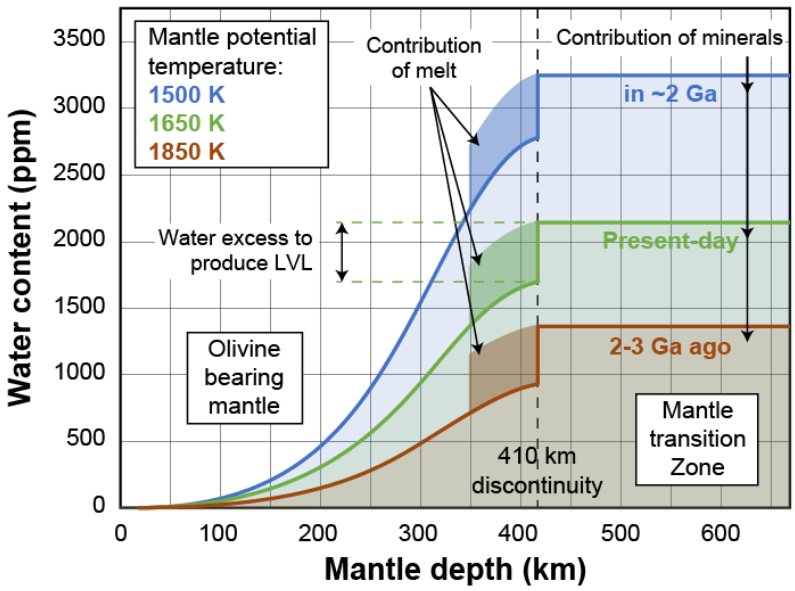

Fig. 7: Water content in the upper mantle as a function of mantle potential temperature. At a depth shallower than 410 km, the H_2O content of the mantle follows the water-saturation profiles (Fig. 1). On the other hand, the water content in the mantle transition zone can be estimated as being the sum of the solubility limit in the mantle above 410 km and the water content needed to produce 0.5 to 1 wt% of hydrous-melt in the low-velocity layer, in agreement with seismic data. The mean thickness of the LVL is ~60 km, but depends on mantle heterogeneities in H_2O and FeO contents, and temperature (see text). The same calculation is performed for mantle potential temperatures of 1850 K (red: 2-3 Ga ago), 1650 K (green: ~present-day) and 1500 K (blue: in the future). Uncertainty on water contents is same as in Fig. 1.

Now we calculate the total amount of water present in the upper mantle (Fig. 7). An OBM close to its water saturation limit yields an integrated value of its water content of ~4.3(0.4) 10^{20} kg or ~0.31(0.03) OM. Added to the 0.6(0.1) OM in the MTZ (see above), we conclude that a water-equivalent of ~1.0(0.1) OM of water currently resides in the mantle above the 660 km discontinuity. We acknowledge that this calculation does not include possible effects associated with an increase in the water solubility limit in the lithospheric mantle and the crust (Green et al., 2014; Mierdel et al., 2007; Sarafian et al., 2017). For estimating a water budget over the entire mantle, the amount of water residing in the lower mantle should also be considered: different experimental works based on high-quality single-crystal of bridgmanite find a radically different water storage capacity from ~100 ppm (Bolfan-Casanova et al., 2003) to ~1000 ppm (Fu et al., 2019), which translates into maxima of ~0.3 to ~3 OM in the lower mantle. Ferropericlase and $CaSiO_3$-perovskite may also integrate minor amounts of H. In addition, some water may be carried below the 660 km discontinuity in dense hydrous phases that remain stable in low-temperature slabs (Nishi et al., 2014; Pamato et al., 2015). Still, partition coefficients greater than 10 between most NAMs and bridgmanite favor the storage of water in the MTZ, compared to the lower mantle (Bolfan-Casanova et al., 2003) and thus we consider that the lower mantle should be fairly dry.

Water budget of the mantle over the Earth's history

We evaluate the amount of water that has been stored in the mantle over the course of the Earth's history. Analyses of ancient non-arc basalts and komatiites suggest a rate of mantle cooling of ~100 K/Ga (e.g. (Herzberg et al., 2010)). A higher mantle temperature in the past implies a lower water storage capacity for NAMs (Fig. 1) and thus less water stored in the upper mantle (Fig. 7). The amount of water stored in the MTZ in the past can be estimated from the maximum water storage capacity of the mantle just above the 410 km discontinuity making following assumptions: (i) the LVL has persisted since the establishment of slab subduction, due to the parental link between subducted water and formation of the LVL (see above). (ii) LVL properties, e.g. its dependence on mantle temperature and water content,

have remained the same over time, which enables the use of the melting diagram (Fig. 4). It implies that the excess water in the MTZ, compared to the OBM, is regulated by the LVL (Fig. 7). In other words, we assume that although the deep water cycle has evolved over the last 2-3 Ga, a stable equilibrium between the flow of water into the MTZ via subduction and the flow of water out the MTZ via melt formed at the LVL was established early on and maintained over geological times. We thus obtain water contents of 930(100) or 2800(300) ppm for the OBM at 410 km depth from Fig. 1, and 1400(200) or 3300(500) ppm for the MTZ, for T_P varying from the highest values of 1850 K (in the past) to 1500 K (in the future), respectively (Fig. 7).

The water storage capacity in the entire upper mantle (above 660 km depth) is found to increase from ~0.6(0.1) to ~1.4(0.2) OM from 2-3 Ga ago (T_P ~1850 K) to a point in the future when T_P will achieve 1500 K (Fig. 8). This corresponds to a net decrease of the water elevation of the oceans by ~900 m in the last 2-3 Ga, for a mean elevation today of 4.5 km. These trends correspond to a decrease of the oceanic mass of ~20% per Ga, in agreement with previous findings of a loss of several 10s % of the OM over geological time, based on hydrogen isotopes (Lecuyer et al., 1998; Pope et al., 2012) and geodynamic modeling (Flament et al., 2013). The mantle storage capacity will continue to increase to a maximum value of ~1.6 OM, when T_P may eventually decrease to 1400 K in several Ga from now.

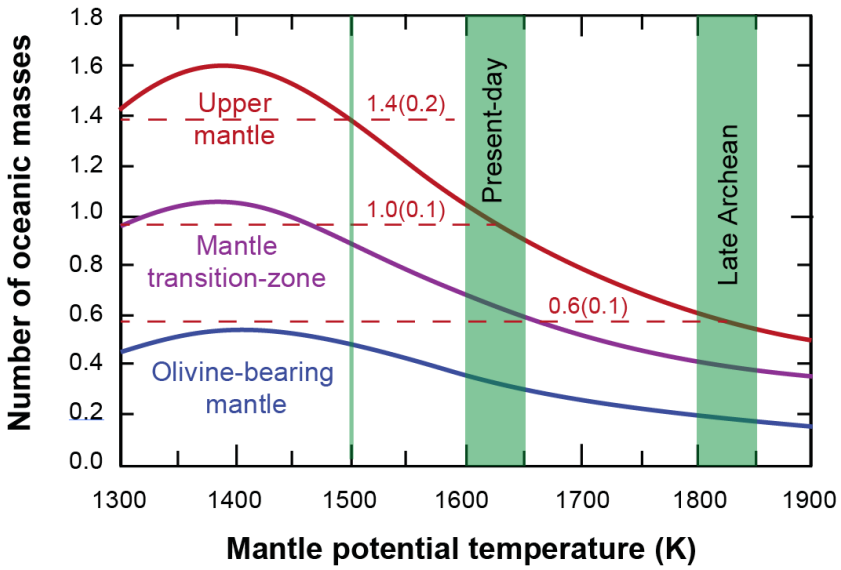

Fig. 8: Water content of upper mantle reservoirs throughout Earth's history. Water contents in the entire upper mantle (red), constituted of the OBM (blue) and of the MTZ (purple), calculated from the integration of water contents as a function of depth (Fig. 7) for various T_P. With present-day T_P ~1650 K, we expect ~1.0(0.1) ocean mass (OM) trapped in the mantle above 660 km (central red dashed line), with ~0.4 and ~0.6 OM in OBM and MTZ, respectively). The water storage capacity in the upper mantle increases with secular cooling at a rate of ~20% of the ocean mass per billion years. Uncertainty is +/-15% similar to that of Fig. 1.

Finally, we investigate the critical amount of water needed to produce a planet like the Earth in terms of the surface ratio between oceans and emerged-continents. For the Earth, the present-day ~2.0 OM (1.0 OM residing at the surface and 1.0 OM in the mantle) stored above the 660 km discontinuity ensures the existence of an ocean at the surface of the planet regardless of its age (i.e. its mantle temperature). During the Archean, the mantle was hotter and thus its water storage capacity was lower, ~0.6 OM, implying a volume of Archean oceans ~1.3 times that of today's. This agrees with inferences, based on the $^{87}Sr/^{86}Sr$ isotopic composition of marine carbonates, that there was little (less than 4%) emerged land 2.5 Ga ago (Flament et al., 2008). With cooling to the present-day potential temperature of 1650 K, the hydrosphere would have been entirely buried into the solid mantle if the total terrestrial water content had been less than ~1.0 OM (Fig. 8). In the future, the water storage capacity of the upper mantle is expected to further increase with secular cooling, possibly reaching a maximum of ~1.6 OM for a mantle potential temperature of 1400 K. This would leave only 0.4 OM at the Earth's surface. Therefore, variations of the total amount of water in the mantle of a planet with the size of the Earth

may easily result in no emerged land early in the history, or the absence of a surface ocean a few Ga after the planet's formation, just because of the interplay with the mantle.

Conclusion

In this article, we develop the "mantle rain" model and its implications. The model is based on the mechanism of dehydration melting taking place above the 410 km discontinuity and producing a water-saturated melt and solid residue, which together form the LVL observed by seismology. Starting from the well-accepted concept of a neutral melt-mantle buoyancy at the upper limit of the LVL, we develop the idea that the LVL is a source for upwelling melts. With such mechanism, it becomes possible to balance the incoming (by subduction) and outgoing (by rise of LVL-melt) water flows for the MTZ. Within the upper mantle, a water-bearing melt is expected to travel several orders of magnitude faster than the mantle residue stirred by convection movements. The melt could travel relatively fast laterally and vertically, favoring homogenization of the water content, mantle refertilisation, seismic anomalies such as the LVZ, intraplate volcanism, etc.

The occurrence of dehydration melting in the LVL also offers a clue to estimate the average water content in the MTZ. It should be higher than the maximum water-storage capacity of the OBM at 410 km depth, 1700(200) ppm, as determined experimentally, and should also account for the continuous production of the water-bearing LVL-melt: thus, it should be ~2200(300) ppm H_2O for Tp of 1650 K. Based on this value and with the idea that the OBM should be almost saturated in water, we find that ~1 ocean mass of water is stored in the entire upper mantle today. The same calculation can be performed for mantle potential temperatures higher (in the past) and lower (in the future) than that of 1600-1650 K prevailing today. With an increasing water storage capacity of the mantle as a function of decreasing mantle temperature, the mass of the oceans at the Earth's surface is found to decrease by 20% every billion years, when considering a rate of mantle cooling of ~100 K/Ga.

Supplementary Material:

Water fugacity in the upper mantle

We calculate the water fugacity (f_{H2O}) of pure water based on the previous equation of state (EoS) of H_2O (Pitzer and Sterner, 1994). However, geological fluids/melts are not pure water, at high pressures above ~3 GPa, as they dissolve a significant amount of silicate at high mantle temperatures (Massuyeau et al., 2015; Mibe et al., 2007). It makes the f_{H2O} significantly lower than that of pure H_2O. To take this effect into account, we apply a correction to the f_{H2O} of pure water based on a previous experimental report of the water content of olivine up to 12 GPa and 1673 K (Suppl. Fig. 1) (Bali et al., 2008):

$$f_{H2O} = f_{H2O}^{\text{Pure-water}} * [1 - A_1 \exp(-\Delta G_1/RT)] \qquad \text{(Suppl-Eq. 1)}$$

with ΔG_1 related to the energy of dissolution of the silicate component in the fluid. ΔG_1 can vary with several parameters, in particular temperature and fluid composition. In order to reproduce the ratio of real water fugacity over that of the pure fluid reported previously (Suppl. Fig. 1; (Bali et al., 2008)), we adopted a ΔG_1 value that decreases exponentially with increasing temperature:

$$\Delta G_1 = A_2 \exp(-\Delta G_2/RT) \qquad \text{(Suppl-Eq. 2)}$$

with A_1=1, A_2=2.50 10^{-2} and ΔG_2=-140 kJ/mol. For convenience, we use this formalism for further modeling of f_{H2O} in supercritical fluids or hydrous melts at upper mantle pressures and temperatures.

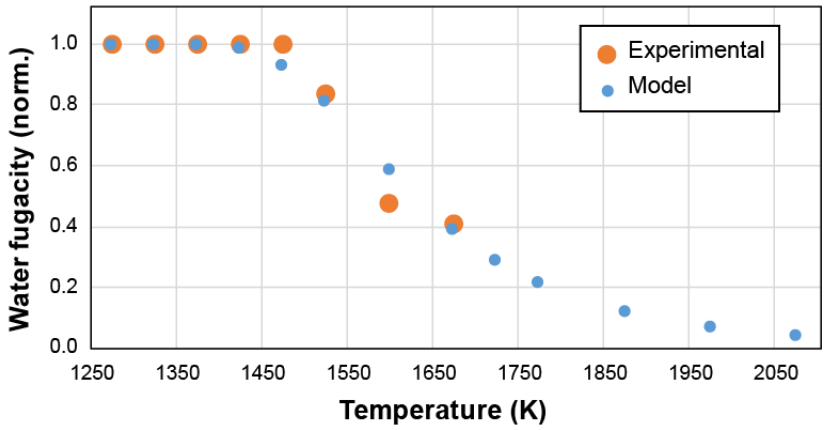

Suppl. Fig. 1: Temperature dependence of water fugacity (i.e. the correction to apply to the f_{H2O} of pure water). Experimental data obtained between 3 and 12 GPa (Bali et al., 2008) are fitted using a double exponential function (Suppl-Eq. 1 and 2). The model reproduces well the amplitude of the f_{H2O} decrease induced by a change of the melt composition (from water-rich to silicate-rich) with increasing the temperature above ~1500 K.

Acknowledgements: We thank E. Debayle and B. Tauzin for major inputs concerning seismic tomography in the upper mantle, P. Condamine for precisions about his sandwich-derived composition of LVL-melt, S. Demouchy, D. Freitas, M. Garçon, D. Laporte, G. Manthilake, E. Médard, M. Monnereau and anonymous reviewers for fruitful discussions. This research was financed by the French Government Laboratory of Excellence initiative n°ANR-10-LABX-0006, the Région Auvergne and the European Regional Development Fund. This is Laboratory of Excellence ClerVolc contribution N°XX.

References cited:

Andrault, D., Pesce, G., Manthilake, G., Monteux, J., Bolfan-Casanova, N., Chantel, J., Novella, D., Guignot, N., King, A., Itie, J.-P., Hennet, L., 2018. Deep and persistent melt layer in the Archaean mantle. Nat. Geosci. 11, 139-+.

Ardia, P., Hirschmann, M.M., Withers, A.C., Tenner, T.J., 2012. H_2O storage capacity of olivine at 5-8 GPa and consequences for dehydration partial melting of the upper mantle. Earth Planet. Sci. Lett. 345, 104-116.

Aubaud, C., Hauri, E.H., Hirschmann, M.M., 2004. Hydrogen partition coefficients between nominally anhydrous minerals and basaltic melts. Geophys. Res. Lett. 31.

Bali, E., Bolfan-Casanova, N., Koga, K.T., 2008. Pressure and temperature dependence of H solubility in forsterite : an implication to water activity in the Earth interior. Earth Planet. Sci. Lett., 354-363.

Bercovici, D., Karato, S., 2003. Whole-mantle convection and the transition-zone water filter. Nature 425, 39-44.

Bolfan-Casanova, N., Keppler, H., Rubie, D.C., 2000. Water partitioning between nominally anhydrous minerals in the MgO-SiO_2-H_2O system up to 24 GPa: implications for the distribution of water in the Earth's mantle. Earth Planet. Sci. Lett. 182, 209-221.

Bolfan-Casanova, N., Keppler, H., Rubie, D.C., 2003. Water partitioning at 660 km depth and evidence for very low water solubility in magnesium silicate perovskite. Geophys. Res. Lett. 30, L017182.

Buchen, J., Marquardt, H., Speziale, S., Kawazoe, T., Boffa Ballaran, T., Kurnosov, A., 2018. High-pressure single-crystal elasticity of wadsleyite and the seismic signature of water in the shallow transition zone. Earth Planet. Sci. Lett. 498, 77-87.

Chantel, J., Manthilake, G., Andrault, D., Novella, D., Yu, T., Wang, Y.B., 2016. Experimental evidence supports mantle partial melting in the asthenosphere. Sci. Adv. 2.

Cogne, J.P., Humler, E., 2006. Trends and rhythms in global seafloor generation rate. Geochem., Geophys., Geosyst. 7.

Condamine, P., Frost, D.J., 2018. Kimberlite from incipient melting of the mantle transition zone?, Annual Report of BGI. Bayerisches Geoinstitute, Bareuth.

Courtillot, V., Davaille, A., Besse, J., Stock, J., 2003. Three distinct types of hotspots in the Earth's mantle. Earth Planet. Sci. Lett. 205, 295-308.

Dasgupta, R., Hirschmann, M.M., 2007. A modified iterative sandwich method for determination of near-solidus partial melt compositions. II. Application to determination of near-solidus melt compositions of carbonated peridotite. Contrib. Mineral. Petr. 154, 647-661.

de Leeuw, N.H., Parker, S.C., Catlow, C.R.A., Price, G.D., 2000. Modelling the effect of water on the surface structure and stability of forsterite. Phys. Chem. Mineral. 27, 332-341.

Debayle, E., Bodin, T., Durand, S., Ricard, Y., 2020. Seismic evidence for partial melt below tectonic plates. Nature 586, 555-559.

Debayle, E., Ricard, Y., 2012. A global shear velocity model of the upper mantle from fundamental and higher Rayleigh mode measurements. J. Geophys. Res. 117.

Demouchy, S., 2010. Hydrogen diffusion in spinel grain boundaries and consequences for chemical homogenization in hydrous peridotite. Contrib. Mineral. Petr. 160, 887-898.

Demouchy, S., Shcheka, S., Denis, C.M.M., Thoraval, C., 2017. Subsolidus hydrogen partitioning between nominally anhydrous minerals in garnet-bearing peridotite. Am. Miner. 102, 1822-1831.

Denis, C.M.M., Alard, O., Demouchy, S., 2015. Water content and hydrogen behaviour during metasomatism in the uppermost mantle beneath Ray Pic volcano (Massif Central, France). Lithos 236-237, 256-274.

Dong, J., Fischer, R.A., Stixrude, L.P., Lithgow-Bertelloni, C.R., 2021. Constraining the Volume of Earth's Early Oceans With a Temperature-Dependent Mantle Water Storage Capacity Model. AGU Advances 2, e2020AV000323.

Doucet, L.S., Peslier, A.H., Ionov, D.A., Brandon, A.D., Golovin, A.V., Goncharov, A.G., Ashchepkov, I.V., 2014. High water contents in the Siberian cratonic mantle linked to metasomatism: An FTIR study of Udachnaya peridotite xenoliths. Geochim. Cosmochim. Acta 137, 159-187.

Druzhbin, D., Fei, H., Katsura, T., 2021. Independent hydrogen incorporation in wadsleyite from oxygen fugacity and non-dissociation of H2O in the reducing mantle transition zone. Earth Planet. Sci. Lett. 557, 116755.

Durand, S., Debayle, E., Ricard, Y., Zaroli, C., Lambotte, S., 2017. Confirmation of a change in the global shear velocity pattern at around 1000km depth. Geophys. J. Int. 211, 1628-1639.

Fei, H., Yamazaki, D., Sakurai, M., Miyajima, N., Ohfuji, H., Katsura, T., Yamamoto, T., 2017. A nearly water-saturated mantle transition zone inferred from mineral viscosity. Sci. Adv. 3.

Ferot, A., Bolfan-Casanova, N., 2012. Water storage capacity in olivine and pyroxene to 14 GPa: Implications for the water content of the Earth's upper mantle and nature of seismic discontinuities. Earth Planet. Sci. Lett. 349, 218-230.

Flament, N., Coltice, N., Rey, P.F., 2008. A case for late-Archaean continental emergence from thermal evolution models and hypsometry. Earth Planet. Sci. Lett. 275, 326-336.

Flament, N., Coltice, N., Rey, P.F., 2013. The evolution of the Sr-87/Sr-86 of marine carbonates does not constrain continental growth. Precambrian Res. 229, 177-188.

Freitas, D., Manthilake, G., Chantel, J., Bouhifd, M.A., Andrault, D., 2019. Simultaneous measurements of electrical conductivity and seismicwave velocity of partially molten geological materials: effect of evolving melt texture. Phys. Chem. Mineral. 46, 535-551.

Freitas, D., Manthilake, G., Schiavi, F., Chantel, J., Bolfan-Casanova, N., Bouhifd, M.A., Andrault, D., 2017. Experimental evidence supporting a global melt layer at the base of the Earth's upper mantle. Nat. Commun. 8.

Frost, D.J., Dolejs, D., 2007. Experimental determination of the effect of H_2O on the 410-km seismic discontinuity. Earth Planet. Sci. Lett. 256, 182-195.

Fu, S., Yang, J., Karato, S.-i., Vasiliev, A., Presniakov, M.Y., Gavriliuk, A.G., Ivanova, A.G., Hauri, E.H., Okuchi, T., Purevjav, N., Lin, J.-F., 2019. Water Concentration in Single-Crystal (Al,Fe)-Bearing Bridgmanite Grown From the Hydrous Melt: Implications for Dehydration Melting at the Topmost Lower Mantle. Geophys. Res. Lett. 46, 10346-10357.

Fukao, Y., Obayashi, M., 2013. Subducted slabs stagnant above, penetrating through, and trapped below the 660 km discontinuity. J. Geophys. Res. 118, 5920-5938.

Gaillard, F., Malki, M., Iacono-Marziano, G., Pichavant, M., Scaillet, B., 2008. Carbonatite Melts and Electrical Conductivity in the Asthenosphere. Science 322, 1363-1365.

Green, D.H., Hibberson, W.O., Rosenthal, A., Kovacs, I., Yaxley, G.M., Falloon, T.J., Brink, F., 2014. Experimental Study of the Influence of Water on Melting and Phase Assemblages in the Upper Mantle. Journal of Petrology 55, 2067-2096.

Greenwood, R.C., Barrat, J.A., Miller, M.F., Anand, M., Dauphas, N., Franchi, I.A., Sillard, P., Starkey, N.A., 2018. Oxygen isotopic evidence for accretion of Earth's water before a high-energy Moon-forming giant impact. Sci. Adv. 4.

Hae, R., Ohtani, E., Kubo, T., Koyama, T., Utada, H., 2006. Hydrogen diffusivity in wadsleyite and water distribution in the mantle transition zone. Earth Planet. Sci. Lett. 243, 141-148.

Herzberg, C., Condie, K., Korenaga, J., 2010. Thermal history of the Earth and its petrological expression. Earth Planet. Sci. Lett. 292, 79-88.

Hier-Majumder, S., Keel, E.B., Courtier, A.M., 2014. The influence of temperature, bulk composition, and melting on the seismic signature of the low-velocity layer above the transition zone. J. Geophys. Res. 119, 971-983.

Hier-Majumder, S., Ricard, Y., Bercovici, D., 2006. Role of grain boundaries in magma migration and storage. Earth Planet. Sci. Lett. 248, 735-749.

Hier-Majumder, S., Tauzin, B., 2017. Pervasive upper mantle melting beneath the western US. Earth Planet. Sci. Lett. 463, 25-35.

Hirschmann, M.M., 2010. Partial melt in the oceanic low velocity zone. Phys. Earth Planet. Inter. 179, 60-71.

Hirschmann, M.M., Aubaud, C., Withers, A.C., 2005. Storage capacity of H_2O in nominally anhydrous minerals in the upper mantle. Earth Planet. Sci. Lett. 236, 167-181.
Huang, X., Xu, Y., Karato, S., 2005. Water content in the transition zone from electrical conductivity of wadsleyite and ringwoodite. Nature 434, 746-749.
Inoue, T., 1994. Effect of water on melting phase relations and melt composition in the system Mg2SiO4□MgSiO3□H2O up to 15 GPa. Phys. Earth Planet. Inter. 85, 237-263.
Irifune, T., Isshiki, M., 1998. Iron partitioning in a pyrolite mantle and the nature of the 410-km seismic discontinuity. Nature 392, 702-705.
Jing, Z., Karato, S.-i., 2012. Effect of H2O on the density of silicate melts at high pressures: Static experiments and the application of a modified hard-sphere model of equation of state. Geochim. Cosmochim. Acta 85, 357-372.
Katsura, T., Yoneda, A., Yamazaki, D., Yoshino, T., Ito, E., 2010. Adiabatic temperature profile in the mantle. Phys. Earth Planet. Inter. 183, 212-218.
Kawakatsu, H., Kumar, P., Takei, Y., Shinohara, M., Kanazawa, T., Araki, E., Suyehiro, K., 2009. Seismic Evidence for Sharp Lithosphere-Asthenosphere Boundaries of Oceanic Plates. Science 324, 499-502.
Kessel, R., Pettke, T., Fumagalli, P., 2015. Melting of metasomatized peridotite at 4-6 GPa and up to 1200 degrees C: an experimental approach. Contrib. Mineral. Petr. 169.
Kohlstedt, D.L., Keppler, H., Rubie, D.C., 1996. Solubility of water in the alpha, beta and gamma phases of (Mg,Fe)(2)SiO4. Contrib. Mineral. Petr. 123, 345-357.
Kuritani, T., Xia, Q.K., Kimura, J., Liu, J., Shimizu, K., Ushikubo, T., Zhao, D.P., Nakagawa, M., Yoshimura, S., 2019. Buoyant hydrous mantle plume from the mantle transition zone. Scientific Reports 9.
Lambart, S., Laporte, D., Schiano, P., 2009. An experimental study of pyroxenite partial melts at 1 and 1.5 GPa: Implications for the major-element composition of Mid-Ocean Ridge Basalts. Earth Planet. Sci. Lett. 288, 335-347.
Le Roux, V., Bodinier, J.L., Tommasi, A., Alard, O., Dautria, J.M., Vauchez, A., Riches, A.J.V., 2007. The Lherz spinel lherzolite: Refertilized rather than pristine mantle. Earth Planet. Sci. Lett. 259, 599-612.
Leahy, G.M., Bercovici, D., 2007. On the dynamics of a hydrous melt layer above the transition zone. J. Geophys. Res. 112.
Lecuyer, C., Gillet, P., Robert, F., 1998. The hydrogen isotope composition of seawater and the global water cycle. Chemical Geology 145, 249-261.
Liu, Z., Fei, H., Chen, L., McCammon, C., Wang, L., Liu, R., Wang, F., Liu, B., Katsura, T., 2021. Bridgmanite is nearly dry at the top of the lower mantle. Earth Planet. Sci. Lett. 570, 117088.
Liu, Z., Park, J., Karato, S.-i., 2016. Seismological detection of low-velocity anomalies surrounding the mantle transition zone in Japan subduction zone. Geophys. Res. Lett. 43, 2480-2487.
Liu, Z., Park, J., Karato, S.-i., 2018. Seismic evidence for water transport out of the mantle transition zone beneath the European Alps. Earth Planet. Sci. Lett. 482, 93-104.
Machida, S., Kogiso, T., Hirano, N., 2017. Petit-spot as definitive evidence for partial melting in the asthenosphere caused by CO2. Nat. Commun. 8.
Mao, Z., Jacobsen, S.D., Jiang, F., Smyth, J.R., Holl, C.M., Duffy, T.S., 2008. Elasticity of hydrous wadsleyite to 12 GPa: Implications for Earth's transition zone. Geophys. Res. Lett. 35.
Marty, B., 2012. The origins and concentrations of water, carbon, nitrogen and noble gases on Earth. Earth Planet. Sci. Lett. 313, 56-66.
Massuyeau, M., Gardés, E., Morizet, Y., Gaillard, F., 2015. A model for the activity of silica along the carbonatite-kimberlite-mellilitite-basanite melt compositional joint. Chemical Geology 418, 206-216.
Matsukage, K.N., Jing, Z.C., Karato, S., 2005. Density of hydrous silicate melt at the conditions of Earth's deep upper mantle. Nature 438, 488-491.
Mibe, K., Kanzaki, M., Kawamoto, T., Matsukage, K.N., Fei, Y.W., Ono, S., 2007. Second critical endpoint in the peridotite-H2O system. J. Geophys. Res. 112.
Mibe, K., Orihashi, Y., Nakai, S., Fujii, T., 2006. Element partitioning between transition-zone minerals and ultramafic melt under hydrous conditions. Geophys. Res. Lett. 33.

Michael, P.J., 1988. The concentration, behavior and storage of H2O in the suboceanic upper mantle: Implications for mantle metasomatism. Geochim. Cosmochim. Acta 52, 555-566.
Mierdel, K., Keppler, H., Smyth, J.R., Langenhorst, F., 2007. Water solubility in aluminous orthopyroxene and the origin of Earth's asthenosphere. Science 315, 364-368.
Mosenfelder, J.L., Deligne, N.I., Asimow, P.D., Rossman, G.R., 2006. Hydrogen incorporation in olivine from 2-12 GPa. Am. Miner. 91, 285-294.
Ni, H., Keppler, H., Behrens, H., 2011. Electrical conductivity of hydrous basaltic melts: implications for partial melting in the upper mantle. Contrib. Mineral. Petr. 162, 637-650.
Nishi, M., Irifune, T., Tsuchiya, J., Tange, Y., Nishihara, Y., Fujino, K., Higo, Y., 2014. Stability of hydrous silicate at high pressures and water transport to the deep lower mantle. Nat. Geosci. 7, 224-227.
Novella, D., Frost, D.J., Hauri, E.H., Bureau, H., Raepsaet, C., Roberge, M., 2014. The distribution of H_2O between silicate melt and nominally anhydrous peridotite and the onset of hydrous melting in the deep upper mantle. Earth Planet. Sci. Lett. 400, 1-13.
O'Reilly, S.Y., Griffin, W.L., 2013. Mantle metasomatism. Metasomatism and the Chemical Transformation of Rock, Lecture Notes in Earth System Sciences. Springer Berlin Heidelberg, pp. 471-533.
Ohtani, E., Mizobata, H., Yurimoto, H., 2000. Stability of dense hydrous magnesium silicate phases in the systems Mg₂SiO₄-H₂O and MgSiO₃-H₂O at pressures up to 27 GPa. Phys. Chem. Mineral. 27, 533-544.
Ohtani, E., Yuan, L., Ohira, I., Shatskiy, A., Litasov, K., 2018. Fate of water transported into the deep mantle by slab subduction. Journal of Asian Earth Sciences 167, 2-10.
Padrón-Navarta, J.A., Hermann, J., 2017. A Subsolidus Olivine Water Solubility Equation for the Earth's Upper Mantle. J. Geophys. Res. 122, 9862-9880.
Pamato, M.G., Myhill, R., Ballaran, T.B., Frost, D.J., Heidelbach, F., Miyajima, N., 2015. Lower-mantle water reservoir implied by the extreme stability of a hydrous aluminosilicate. Nat. Geosci. 8, 75-79.
Pearson, D.G., Brenker, F.E., Nestola, F., McNeill, J., Nasdala, L., Hutchison, M.T., Matveev, S., Mather, K., Silversmit, G., Schmitz, S., Vekemans, B., Vincze, L., 2014. Hydrous mantle transition zone indicated by ringwoodite included within diamond. Nature 507, 221-+.
Piani, L., Marrocchi, Y., Rigaudier, T., Vacher, L.G., Thomassin, D., Marty, B., 2020. Earth's water may have been inherited from material similar to enstatite chondrite meteorites. Science 369, 1110-+.
Pitzer, K.S., Sterner, S.M., 1994. Equation of state valid continuously from zero to extreme pressures for H_2O and CO_2. J. Chem. Phys. 101, 3111-3116.
Pope, E.C., Bird, D.K., Rosing, M.T., 2012. Isotope composition and volume of Earth's early oceans. Proc. Natl. Acad. Sci. U. S. A. 109, 4371-4376.
Priestley, K., McKenzie, D., 2013. The relationship between shear wave velocity, temperature, attenuation and viscosity in the shallow part of the mantle. Earth Planet. Sci. Lett. 381, 78-91.
Revenaugh, J., Jordan, T.H., 1991. Mantle layering from SCS reverberations 3. The upper mantle. J. Geophys. Res. 96, 19781-19810.
Revenaugh, J., Sipkin, S.A., 1994. Seismic evidence for silicate melt atop the 410 km mantle discontinuity. Nature 369, 474-476.
Rupke, L.H., Morgan, J.P., Hort, M., Connolly, J.A.D., 2004. Serpentine and the subduction zone water cycle. Earth Planet. Sci. Lett. 223, 17-34.
Sakamaki, T., Suzuki, A., Ohtani, E., 2006. Stability of hydrous melt at the base of the Earth's upper mantle. Nature 439, 192-194.
Sarafian, E., Gaetani, G.A., Hauri, E.H., Sarafian, A.R., 2017. Experimental constraints on the damp peridotite solidus and oceanic mantle potential temperature. Science 355, 942-944.
Schmandt, B., Jacobsen, S.D., Becker, T.W., Liu, Z.X., Dueker, K.G., 2014. Dehydration melting at the top of the lower mantle. Science 344, 1265-1268.
Shirey, S.B., Wagner, L.S., Walter, M.J., Pearson, D.G., van Keken, P.E., 2021. Slab Transport of Fluids to Deep Focus Earthquake Depths—Thermal Modeling Constraints and Evidence From Diamonds. AGU Advances 2, e2020AV000304.

Smyth, J.R., Frost, D.J., Nestola, F., Holl, C.M., Bromiley, G., 2006. Olivine hydration in the deep upper mantle: Effects of temperature and silica activity. Geophys. Res. Lett. 33.
Soltanmohammadi, A., Gregoire, M., Rabinowicz, M., Gerbault, M., Ceuleneer, G., Rahgoshay, M., Bystricky, M., Benoit, M., 2018. Transport of Volatile-rich Melt from the Mantle Transition Zone via Compaction Pockets: Implications for Mantle Metasomatism and the Origin of Alkaline Lavas in the Turkish-Iranian Plateau. Journal of Petrology 59, 2273-2309.
Song, T.R.A., Helmberger, D.V., Grand, S.P., 2004. Low-velocity zone atop the 410-km seismic discontinuity in the northwestern United States. Nature 427, 530-533.
Stagno, V., Ojwang, D.O., McCammon, C.A., Frost, D.J., 2013. The oxidation state of the mantle and the extraction of carbon from Earth's interior. Nature 493, 84-88.
Swain, M.V., Atkinson, B.K., 1978. Fracture surface-energy of olivine. Pure and Applied Geophysics 116, 866-872.
Tauzin, B., Debayle, E., Wittlinger, G., 2010. Seismic evidence for a global low-velocity layer within the Earth's upper mantle. Nat. Geosci. 3, 718-721.
Toffelmier, D.A., Tyburczy, J.A., 2007. Electromagnetic detection of a 410-km-deep melt layer in the southwestern United States. Nature 447, 991-994.
Toplis, M.J., 2005. The thermodynamics of iron and magnesium partitioning between olivine and liquid: criteria for assessing and predicting equilibrium in natural and experimental systems. Contrib. Mineral. Petr. 149, 22-39.
van Keken, P.E., Hacker, B.R., Syracuse, E.M., Abers, G.A., 2011. Subduction factory: 4. Depth-dependent flux of H_2O from subducting slabs worldwide. J. Geophys. Res. 116.
Vinnik, L., Farra, V., 2007. Low S velocity atop the 410-km discontinuity and mantle plumes. Earth Planet. Sci. Lett. 262, 398-412.
Wang, X.-C., Wilde, S.A., Li, Q.-L., Yang, Y.-N., 2015. Continental flood basalts derived from the hydrous mantle transition zone. Nat. Commun. 6, 7700.
Wen, L.X., Anderson, D.L., 1995. The fate of slabs inferred from seismic tomography and 130 million years of subduction. Earth Planet. Sci. Lett. 133, 185-198.
Xiao, J., Hier-Majumder, S., Tauzin, B., Waltham, D., 2020. An inversion approach for analysing the physical properties of a seismic low-velocity layer in the upper mantle. Phys. Earth Planet. Inter. 304.
Yang, X., 2016. Effect of oxygen fugacity on OH dissolution in olivine under peridotite-saturated conditions: An experimental study at 1.5–7GPa and 1100–1300°C. Geochim. Cosmochim. Acta 173, 319-336.
Yoshino, T., Manthilake, G., Matsuzaki, T., Katsura, T., 2008. Dry mantle transition zone inferred from the conductivity of wadsleyite and ringwoodite. Nature 451, 326-329.
Yoshino, T., Nishihara, Y., Karato, S., 2007. Complete wetting of olivine grain boundaries by a hydrous melt near the mantle transition zone. Earth Planet. Sci. Lett. 256, 466-472.
Zhang, Z., Dueker, K.G., Huang, H.-H., 2018. Ps mantle transition zone imaging beneath the Colorado Rocky Mountains: Evidence for an upwelling hydrous mantle. Earth Planet. Sci. Lett. 492, 197-205.
Zhao, Y.H., Ginsberg, S.B., Kohstedt, D.L., 2004. Solubility of hydrogen in olivine: dependence on temperature and iron content. Contrib. Mineral. Petr. 147, 155-161.